Pressure-induced structural evolution with suppression of the charge density wave state and dimensional crossover in $CeTe_3$

Junlong Li,[1,2,3] Jiajia Feng,[2] Dong Wang,[2] Shang Peng,[2] Mei Li,[2] Hao Wang,[2] Yixuan Xu,[1,3] Tingting Zhao,[2] Bohao Zhao,[2] Sheng Jiang,[4] Xiaodong Li,[1] Chuanlong Lin,[2,*] and Yanchun Li[1,†]

[1]*Multidisciplinary Research Center, Institute of High Energy Physics, Chinese Academy of Science, Beijing 100049, China*

[2]*Center for High Pressure Science and Technology Advanced Research (HPSTAR), Beijing 100094, China*

[3]*University of Chinese Academy of Sciences, Beijing 100049, China*

[4]*Shanghai Advanced Research Institute, Chinese Academy of Science, Shanghai 201210, China*

(Received 25 October 2023; revised 26 February 2024; accepted 8 March 2024; published 27 March 2024)

We present the structural evolution and electrical transport properties in quasi-two-dimensional layered $CeTe_3$ under high pressures by employing Raman spectra, synchrotron x-ray diffraction (XRD), and electrical resistance measurements. Our Raman and XRD experiments reveal the suppression of charge density wave (CDW) occurring via two distinct ways at ∼6 GPa in different hydrostatic environments, namely, incommensurate-to-commensurate transition via the distortion of the Te sheets at quasihydrostatic condition and the transformation from the superlattice of the *Cmcm* structure to an intermediate phase (HP I) with lower symmetric structure at nonhydrostatic condition. The electrical transport measurements show the emergence of the superconductivity (SC) at ∼3.3 GPa after suppression of CDW and antiferromagnetism. Upon further compression up to ∼90 GPa, the low-pressure layered structure transforms into a high-pressure phase (HP II) with three-dimensional structure, which is tentatively attributed to the *Pmmn* symmetry and accompanied by a new superconducting behavior. Our discoveries shed light on the distinct mechanisms in pressure-induced suppression of CDW and transformation from the layered to three-dimensional structure in the rare-earth tritelluride family.

DOI: 10.1103/PhysRevB.109.094119

I. INTRODUCTION

The rare-earth tritelluride family (RTe_3, R=La-Nd, Sm, Gd-Tm, Y) with a quasi-two-dimensional layered structure has attracted increasing attention owing to charge density waves (CDWs), spin density waves, superconductivity, magnetic order and other advanced quantum properties [1–6]. Among the exotic physical properties, the CDW state, characterized by a cooperative periodic modulation of the charge density and crystal lattice, receives special care as a promising model system to study the electron-lattice interplay in the layer structure [7,8]. It originates from the strong coupling between the electronic and lattice degrees of freedom, and can be tuned by modifying the lattice with high pressure, chemical pressure, uniaxial stress, and pump laser [4,9–15]. For example, uniaxial stress can reversibly switch the direction of the ordering wave vector between two in-plane directions by tuning RTe_3 beyond a quasitetragonal structure [11]. Applied pressures can shrink the pseudotetragonal lattice to inhibit the formation of the CDW condensate [9,10,14], while chemical intercalation provides a weak random potential to smear the two CDW transitions into crossovers via chemical pressure, i.e., suppressing long-range CDW order by introducing disordering [16]. The time-dependent CDW domain walls perpendicular to the sample surface will break the CDW long-range order when pump laser is applied, controlled experimentally by the x-ray incidence angle [12,15]. High pressure is often used as a clean method to tune the lattice structure and electronic properties. It plays a crucial role in the modulation of electronic properties in RTe_3, as some intriguing physical phenomena may emerge such as suppression of CDW, superconductivity, magnetic ordering, incommensurate-to-commensurate transition, structural transition from a layered to a three-dimensional (3D) state, etc. [17–24]. Here, we chose $CeTe_3$ as an example to study the structural transitions and electronic transport for understanding the relationship between electronic properties and crystal structure at high pressures.

The crystal structure and electronic properties of rare-earth tritelluride, e.g., CDW and superconductivity, have been extensively investigated under high pressures at various hydrostatic conditions via single-crystal x-ray diffraction (XRD), Raman, reflectivity, and electrical resistance measurements [9,14,25,26]. However, fundamental mechanisms remain vague regarding the electron-lattice interplay. In $CeTe_3$, the intensities of the superlattice diffraction peaks, attributed to CDW, gradually reduced with increasing pressure in the hydrostatic environments with He as the pressure medium, and disappeared at 3 GPa according to single-crystal x-ray diffraction [9]. The distortion of the square-planar Te sheets was observed to be suppressed under compression up to ∼6 GPa with the reduction of the difference between the a and c axes. These results suggested a transition from an incommensurate to commensurate lattice with suppression

*Corresponding author: chuanlong.lin@hpstar.ac.cn
†liyc@ihep.ac.cn

of CDW, which was further supported by low-temperature Raman and reflectivity measurements under quasihydrostatic or hydrostatic conditions [10,14]. When compressed up to 6 GPa, Sacchetti *et al.* [9] reported $CeTe_3$ maintained its *Cmcm* structure without changing its structural symmetry in the XRD and Raman measurements. However, Zocco *et al.* [25] provided the evidence for two magnetic phases at high pressures and low temperatures, and indicated a possible structural transition of $CeTe_3$ at ∼4.5 GPa in the electrical resistivity and specific-heat measurements at quasihydrostatic condition with solid steatite as the pressure medium, showing the discrepancy from the results in the XRD and Raman measurements. This suggests the pressure medium used in the experiments may affect outcomes. Fundamental issues regarding pressure-induced structural transition, mechanism for the suppression of CDW, and change of electronic properties remain unexplored as of yet.

On the other hand, it was reported that some RTe_3 materials, e.g., $GdTe_3$, $TbTe_3$, and $DyTe_3$, become superconductors with a critical temperature of T_c at ∼1 K and ∼2 GPa, following the pressure-induced suppression of CDW [26,27]. Zocoo *et al.* [27] believed that the formation of superconductivity may be closely related to the pressure-induced modulation of the magnetism of the *R*-Te layers and the CDW states. However, the specific mechanism remains controversial. For $CeTe_3$, the previous experiments show no signs of superconductivity under compression up to 16 GPa at 1.6 K despite the suppression of the CDW state at 6 GPa [27,28]. Therefore, further studies are needed to investigate whether superconductivity can be achieved in $CeTe_3$ at high pressure after suppression of CDW. Additionally, the pressure-induced structural transformation from a layered two-dimensional (2D) to a 3D structure has been observed in other layered materials, such as in TaS_2 and CsV_3Sb_5 [17,22,23], accompanied by a reenhanced superconducting phase or domelike superconducting phase. However, it is unknown whether a similar transformation occurs in $CeTe_3$. In this work, we investigated the crystal structural evolution and electronic properties at high pressures by using *in situ* angle dispersive x-ray diffraction, Raman, and electrical transport measurements at quasihydrostatic/nonhydrostatic conditions. Interestingly, our observations reveal two paths responsible for the suppression of CDW at ∼6 GPa and transformation from the layer to three-dimensional structure at high pressure, accompanied by the appearance of two superconducting states.

II. EXPERIMENTAL DETAILS

A. Synthesis method

Single crystals of $CeTe_3$ were synthesized by the binary melt method as described previously [5]. Briefly, elemental cerium metal (99.9%) and tellurium (Alfa Aesar, 99.99%) were mixed with the molar ratio of 1:30 and then vacuum sealed in quartz tubes. The mixtures were heated up to 900 °C to form molten mixtures of Te and $CeTe_3$ and kept for 24 h. Subsequently, the molten $CeTe_3$ were slowly cooled down to 820–870 K over a period of 5 days. The shiny brittle crystal $CeTe_3$ with golden color was separated from liquid tellurium in a centrifuge. The energy dispersive x-ray spectrometry shows the 1:3 ratio and homogeneous distribution of cerium and tellurium in the elemental mapping (Supplemental Material Fig. 1 [29]). The crystal structure at ambient conditions was characterized by the high-resolution transmission electron microscopy (HRTEM), showing the high-quality crystallinity synthesized. The HRTEM images also show some defects may form during the sample preparation for high-pressure experiments (Supplemental Material Fig. 2).

B. Low-temperature Raman experiments

High-pressure Raman experiments at low temperatures were performed in backscattering geometry using a micro spectrometer in the symmetric diamond-anvil cell [30,31]. The diamond-anvil cell (DAC) with 500 μm anvil culet was used in low-temperature Raman measurement. A stainless-steel gasket was preindented to a thickness of 35 μm and a hole was drilled at its center to a diameter of 300 μm. The crystal samples without oxide layers for the experiments were prepared by the tape-based mechanical exfoliation method. A small sample piece with a typical dimensional size of about $50 \times 50 \times 10\,\mu m^3$ was loaded into the sample chamber with one ruby ball as pressure calibrant [32]. Silicone oil served as a pressure-transmitting medium at quasihydrostatic condition. After sample loading, the DAC was placed in a Janis ST-500 continuous flow cryostat. Before cooling, a vacuum pump was used to obtain a vacuum environment. The sample was cooled using a recirculating helium gas cooler, in which helium gas passed through heat exchangers on a cryocooler and flowed into the cryostat to cool the sample. It then returned to the cryocooler for recooling and circulating. The temperature at 10–300 K was monitored by the silicon diode sensor. The Raman spectra were collected in a MonoVista CRS+ system with 532 nm laser excitation and laser power of 0.912 mW. A grating of 2400 grooves/mm was employed throughout the experiment with a collection time of 300 s [33].

C. High-pressure synchrotron x-ray diffraction experiments

In situ angle dispersive x-ray diffraction was performed at the 4W2 beamline of Beijing Synchrotron Radiation Facility and the 15U1 Station of Shanghai Synchrotron Radiation Facility [34]. The x-ray beam of the 4W2 beamline with a wavelength of 0.6199 Å was used and focused into 35×10 μm^2 spots on the sample with K-B mirrors, and the beam of the 15U1 Station with a wavelength of 0.6199 Å was focused into 2×2 μm^2 spots on the sample. The DACs with an anvil culet of 300 μm were used for the high-pressure XRD measurements. The diameter of the sample chamber was ∼120 μm in a stainless-steel gasket that was preindented to ∼30 μm thickness. A piece of sample with a typical dimensional size was loaded into the chamber together with ruby balls serving as the pressure marker [32]. Silicone oil was used to achieve a quasihydrostatic pressure environment (Supplemental Material Fig. 3). The sample kept the initial shape and orientation during the compression process at least up to 10 GPa, indicating a good quasihydrostatic environment provided by the silicone oil (Supplemental Material Fig. 3). It should be noted that $CeTe_3$ has a layered structure and exhibits

a certain degree of brittleness with anisotropic compressibility and relatively small elastic modulus, rendering it vulnerable and prone to distortion under even small deviatoric stress (Supplemental Material Fig. 3). Therefore, the slight stress may have significant influence on the structural evolution of $CeTe_3$. Thus, the nonhydrostatic experiments were conducted without pressure medium, in which the DACs with an anvil culet of 100 μm were employed to provide pressure close to 1 Mbar. Rhenium was used as a gasket with a chamber of 50 μm diameter and the pressure marker [35]. Pressure was controlled by the membrane system in both quasihydrostatic and nonhydrostatic experiments. Two-dimensional (2D) diffraction images were collected with a PILATUS detector with the typical exposure time of 200 s at 4W2 and 30 s at 15U1. During experimental data collection, the DAC was rotated with ±15° along a vertical axis perpendicular to the x-ray beam. The 2D diffraction images were integrated using the DIOPTAS software [36]. The system was calibrated by a CeO_2 standard. Full profile refinements of the XRD patterns were conducted to obtain unit cell parameters by the General Structures Analysis System (GSAS) package [37].

D. High-pressure electrical transport experiments

High-pressure electrical transport measurements were carried out using the standard four-probe method in a nonmagnetic BeCu alloy DAC with a 100 μm anvil culet. The Pt foil was cut into long wires with diameter of 5 μm and used as electrodes. A nonmagnetic rhenium gasket was used with an initial thickness of 200 μm. The preindented hole was covered by cubic boron nitride as the insulating layer with a thickness of ∼20 μm. Subsequently, a hole with 60 μm diameter was drilled by a laser drilling machine as the sample chamber. A piece of sample with a typical dimensional size of $\sim 40 \times 40 \times 20\ \mu m^3$ was loaded into the sample chamber without a pressure-transmitting medium in nonhydrostatic experiments. A ruby ball was loaded for a pressure maker below 50 GPa. The pressure was determined by the Raman shift of diamond above 50 GPa [38]. The prepared DAC was placed in a commercial physical property measurement system (PPMS, Quantum Design and Physike) with automatic temperature control. The electrical transport measurements were performed in a PPMS with the lowest cooling temperature down to 1.6 K and a maximum magnetic field parallel to the *b* axis of the sample up to 9 T.

III. EXPERIMENTAL RESULTS AND DISCUSSION

$CeTe_3$ crystallizes in an orthorhombic structure with *Cmcm* space group at ambient conditions. The x-ray diffraction shows the lattice parameters of $a = 4.3576(5)$ Å, $b = 25.6721(9)$ Å, and $c = 4.3798(7)$ Å at 0.7 GPa, close to previous reports [3] (Supplemental Material Fig. 4). It has a layered structure consisting of alternate stacking corrugated CeTe slabs and double square-planar Te sheets with the Te-Te distance of ∼3.1 Å perpendicular to the *b* axis [Fig. 1(a)]. The Te sheets are bonded weakly by van der Waals interactions with the layered nature in $CeTe_3$. The orthorhombic structure is modulated by the CDW, leading to a distorted square and forming an orthorhombic net in the Te sheets. The HRTEM image demonstrates two kinds of Te-Te bond distances with values of ∼3.08 and ∼3.14 Å in the distorted square Te net [Fig. 1(b)], consistent with the previous studies [3,39–41]. Moreover, a glide plane exists between the two Te sheets along the *c*-axis direction, resulting in a slight difference between lattice *a* and lattice *c*. In order to verify the features of the CDW, selected area electron diffraction was carried out [Fig. 1(c) and Supplemental Material Fig. 5]. The dominant electron diffraction spots of the high-quality single crystal correspond to the *Cmcm* orthorhombic structure. The satellite-weak peaks are attributed to the CDW reflection spots [labeled by red dashed circles in Fig. 1(c)], which come from the modulation of the period lattice with a single in-plane wave vector [$q_{CDW} \approx (2/7)\ c^*$, $c^* = 2\pi/c$]. The satellite-weak peaks indicate an incommensurate lattice in $CeTe_3$ at room temperature, confirming the previous report [4] that the charge density wave modulates the layered orthorhombic structure of $CeTe_3$. The wave vectors of the CDW are calculated to be ∼4.27 nm^{-1}.

Raman experiments further confirm the existence of CDW and modulation of the orthorhombic structure, which evolves with temperature and pressure. Figure 2 shows the Raman-scattering spectra of $CeTe_3$ at various temperatures and pressures. At 295 K and 0.1 GPa in Fig. 2(a), four main peaks are observed at 69, 83, 94, and 109 cm^{-1} (labeled by R1, R2, R3, and R4). The factor group analysis gives the Raman-active phonons of $4A_{1g} + 4B_{1g} + 4B_{3g}$ for the undistorted orthorhombic structure [42]. The R1 and R3 bands are assigned to the A_{1g} mode, corresponding to the vibration of the Te planes; R2 is $A_{1g} + B_{1g}$ mode, originating from the vibration of the Te plane and the CeTe slab; R4 corresponds to the B_{1g} mode owing to the stretching of the Te-Ce bond. Notably, the shoulder peaks exist at around R2 and R4, and a new peak at round 107 cm^{-1} splits from the R4 upon cooling. According to the previous studies [10,42,43], the peak splitting and new peaks emerging near the R2 and R4 bands are attributed to the distorted orthorhombic structure modulated by the CDW. Upon cooling, all the Raman bands become sharper with the reduction of the linewidth (Supplemental Material Fig. 6) and the relative intensities increase as temperature decreases, demonstrating the enhancement of the CDW order in the layered structure of $CeTe_3$ [44].

Upon compression at quasihydrostatic condition [Figs. 2(b)–2(d)], all the Raman bands shift to high wave numbers, associated with the broadening and decrease of the intensities. We note that the R2 band, related to the CDW, splits into two peaks above 1.5 GPa. This implies enhanced distortion of the Te sheets in the modulated tetragonal structure at high pressure [42]. Upon further compression up to ∼6 GPa, the major Raman bands disappear eventually, indicating a pressure-induced structural change and suppression of CDW. This is in agreement with previous studies [10]. Based on present and previous studies [10,41], however, it remains unknown regarding the mechanism for the suppression of CDW and detailed information on the structural evolution at high pressure.

Raman measurements demonstrate the pressure-induced suppression of CDW at ∼6 GPa, which may be related to the structural transition. In order to confirm it, we conducted *in situ* high-pressure x-ray diffraction experiments on

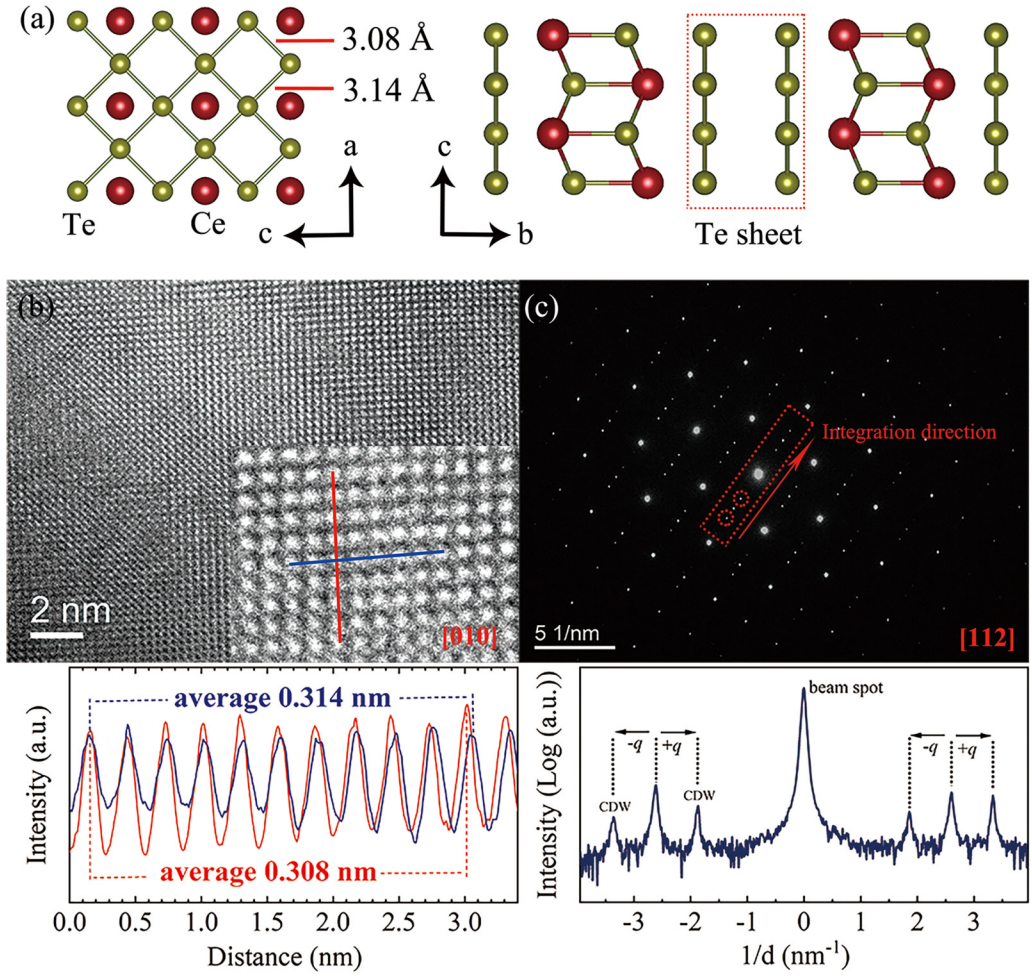

FIG. 1. (a) Crystal structure of $CeTe_3$. (b) Typical HRTEM image of the $CeTe_3$ single crystal along the [010] direction. The intensity scans along red and blue lines show the variation of the Te-Te distances in the Te sheets. (c) Selected area electron diffraction pattern for $CeTe_3$ along the [112] direction. The integral area is marked by the red dashed line, and the intensity integration along the red arrow indicates the satellite peaks attributed to the CDW modulation.

$CeTe_3$ at different hydrostatic conditions. These experiments reveal two distinct pathways in the structural evolutions in the low-pressure range below 19 GPa, namely, structural phase transformation to a lower symmetry structure at nonhydrostatic condition and distortion of Te sheets without structural symmetry broken at quasihydrostatic condition. This implies the suppression of CDW could be caused by two distinct ways.

The comparison of the structural evolutions of $CeTe_3$ during compression from 0 to 19 GPa in nonhydrostatic and quasihydrostatic environments is shown in Fig. 3. Upon compression at nonhydrostatic condition, all peaks shift to higher angles, corresponding to the shrinkage of the lattice planes [Figs. 3(a) and 3(c)]. The original phase is found to be stable up to 6 GPa. Starting from 6.3 GPa, new diffraction peaks arise at 14.7° and 14.9° [marked by arrows in Fig. 3(a)] and persist at least up to 19 GPa, indicating a structural transition at ~6.3 GPa and corresponding to the suppression of CDW. It should be emphasized that the majority of the original diffraction peaks remain without significant changes of the relative intensities in the pressure ranges of 6–19 GPa. This implies $CeTe_3$ still keeps the original layer structure, but with structural symmetry broken. Based on the present XRD data, we cannot solve the crystal structure of the new high-pressure phase (marked as HP I). Upon compression from 0 to 19 GPa at quasihydrostatic condition with silicone oil as the pressure medium, in contrast, $CeTe_3$ keeps *Cmcm* structures without the appearance of new diffraction peaks except for a shift of all the diffraction peaks to higher angles. This means $CeTe_3$ adopts a different path for the structural evolution at quasihydrostatic condition from that at nonhydrostatic condition.

The lattice parameters and the ratio of *a*/*c* for *Cmcm* structures are illustrated in Figs. 3(c) and 3(d). At quasihydrostatic condition, the lattices *a*, *b*, and *c* exhibit different compressibility under compression, indicating anisotropic compression behavior. The ratio of *a*/*c* decreases with increasing pressure. This implies a larger difference between *a* and *c* for the *Cmcm* structure when pressure is increased. As studied in previous work [9], the *a* and *c* axes in the *Cmcm* structure are related to the Te-Te bond distance in the Te sheets [Fig 1(a)]. The difference between *a* and *c* derives from the distortion of the Te sheets due to the modulation of the incommensurate CDW. The larger difference at higher pressure means more distortion of the Te sheets [9]. Additionally, an anomalous compression

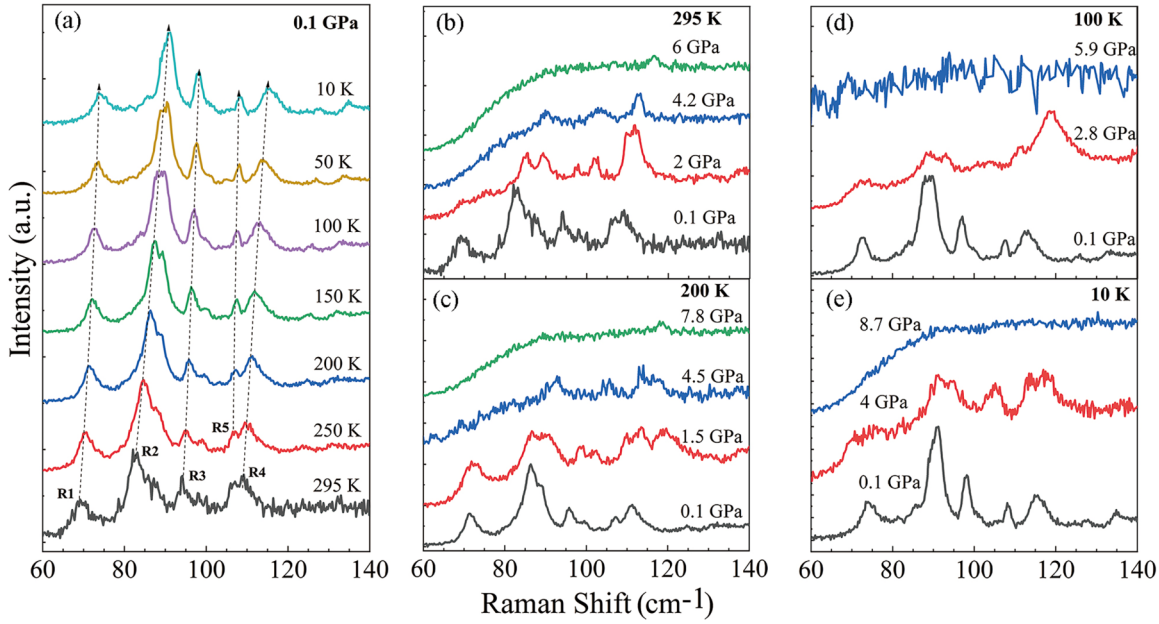

FIG. 2. (a) Raman spectra at 0.1 GPa for the $CeTe_3$ from 295 to 10 K (dashed lines show the Raman bands shifting upon cooling). (b)–(e) The evolution of Raman spectra with increasing pressures at 295, 200, 100, and 10 K, respectively. R1–R5 are Raman symmetry modes marked as references [10]. Pressure was determined by ruby [31].

behavior is observed at ∼6 GPa in the pressure dependence of the lattice parameters and *a*/*c*, where CDW disappears completely. Since the CDW derives from the modulated distortion in the Te sheets along the *a* or *c* axis and corresponds to the incommensurate lattice, the large distortion of the Te sheets may lead to the breaking of the incommensurate lattice with the suppression of CDW at ∼6 GPa, but without structural phase transition observed at quasihydrostatic condition. Straquadine *et al.* [11] give a clue that the CDW of the *Cmcm* $CeTe_3$ can be regulated by changing the ratio of axes *a* and *c*, and be suppressed with *a*/*c* beyond a certain range with the large strain. It indicates the stress has an effect on the Te sheets and can break the weak orthorhombicity structure in the Te sheets, leading to suppression of CDW [9,11]. Obviously, the mechanism of suppression of CDW in Straquadine's work is consistent with that at hydrostatic condition in the present work. The full width at half maximum of the diffraction (111) peak for the *Cmcm* structure of $CeTe_3$ and azimuthally unrolled images

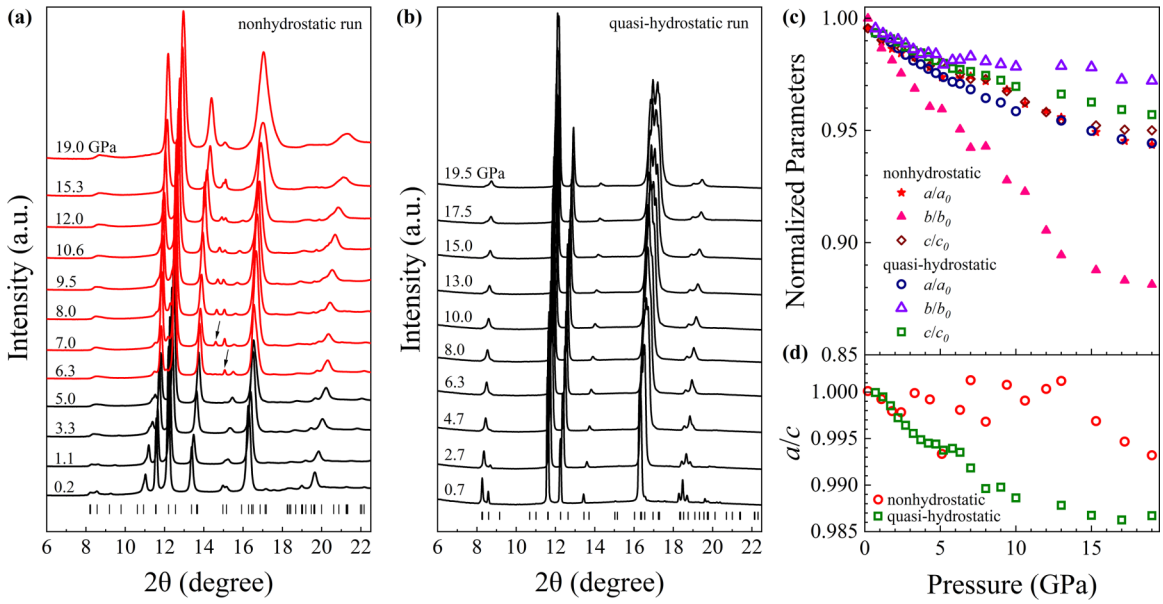

FIG. 3. Structural evolution of $CeTe_3$ in x-ray diffraction measurements under high pressures up to 19 GPa at nonhydrostatic condition (a) and quasihydrostatic condition (b). The black vertical sticks represent the index of the original *Cmcm* structure. (c) Lattice parameters and (d) *a*/*c* as a function of pressure. Rubies were used as pressure markers in both nonhyrostatic and quasihydrostatic environments [31].

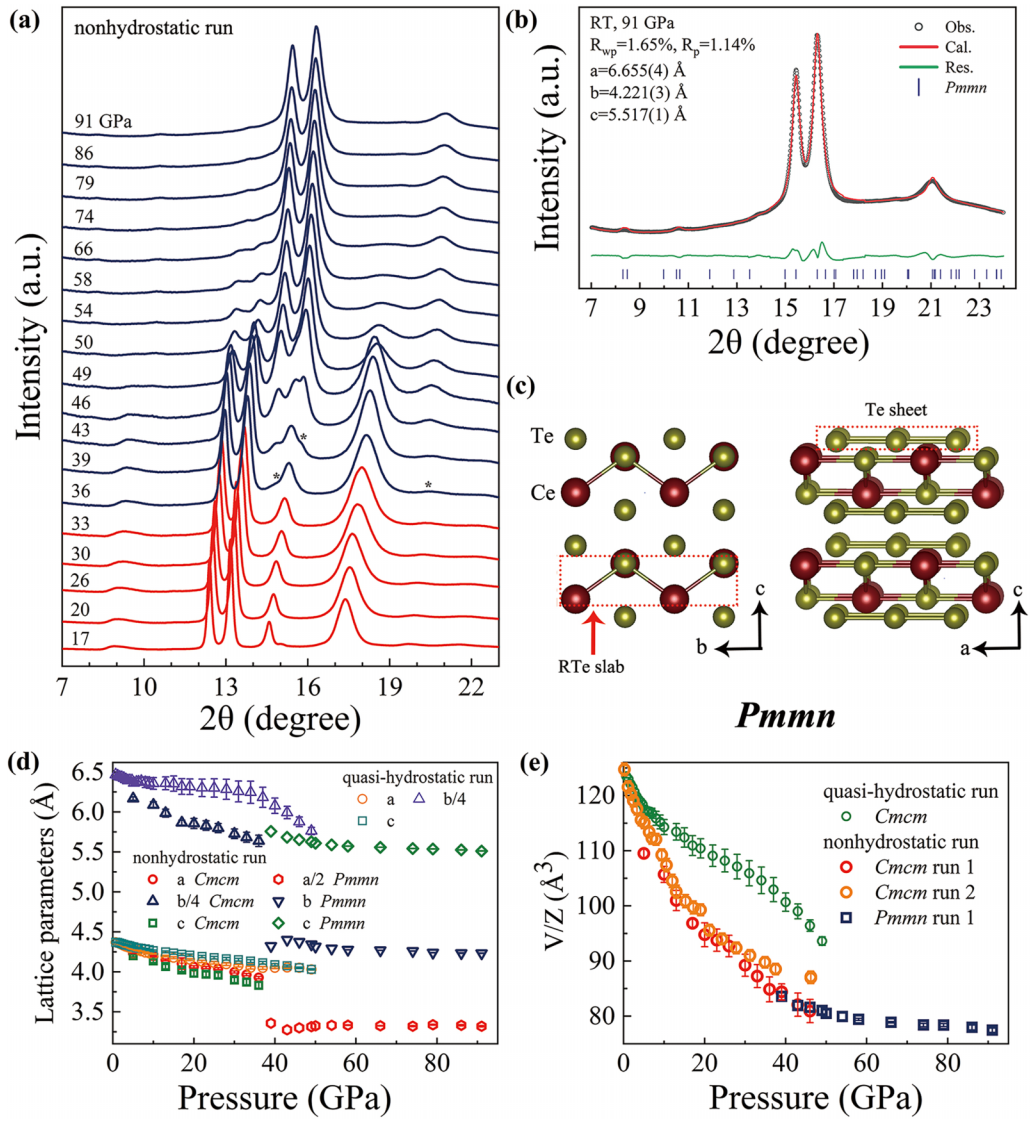

FIG. 4. (a) Structural evolution of $CeTe_3$ in x-ray diffraction measurements from 17 to 91 GPa. (b) The bail fitting of the diffraction pattern of $CeTe_3$ at 91 GPa with the *Pmmn* structure. (c) The tentative schematics of the *Pmmn* structure. (d) The lattice parameters and (e) volume per formula varying with pressure in quasihydrostatic and nonhydrostatic runs. The lattice parameters of the *Cmcm* structures at nonhydrostatic condition were calculated using the main diffraction peaks of the original *Cmcm* structures. Pressures were calculated by ruby and Re [31,34].

of the original 2D diffraction patterns further confirm the large deviatoric stress in the nonhydrostatic environment (Supplemental Material Fig. 7).

Unlike the quasihydrostatic condition, the structural phase transition is observed at ~6 GPa at nonhydrostatic condition. From the present x-ray diffraction data, we cannot give the crystal structure of the new phase and identify whether the diffraction peaks, which exist in the pressure range of 6–19 GPa, belong to the original *Cmcm* structure or to the new phase. The new phase should have lower symmetry, as some weak diffraction peaks are observed. For comparison between quasi- and nonhydrostatic conditions, we attribute the main diffraction peaks to the original *Cmcm* structure and calculate the lattice parameters *a*, *b*, and *c*. The different compressibility and ratio of *a*/*c* are obtained, as shown in Fig. 3(c). The *b* axis at nonhydrostatic condition is more compressible than those of the *a* and *c* axes with a slight change of *a*/*c*, while each axis has close relative compressibility with the decrease of *a*/*c* at pressures below 6 GPa. The significant difference in the compressibility between the *b* axis and the *ac* plane (or Te sheet) in the nonhydrostatic environment may be responsible for the structural distortion and phase transition. This means the structural phase transition with suppression of CDW at nonhydrostatic conditions comes from a different mechanism, rather than only the distortion of the Te sheets as observed at quasihydrostatic condition.

The structural variations of $CeTe_3$ were further investigated at pressures over 19 GPa [Fig. 4(a)]. The primary diffraction peaks of the initial *Cmcm* phase continue to exist up to 36 GPa with the shift to higher angles (Supplemental Material Fig. 8). The appearance of new diffraction peaks (marked by asterisks) and a decrease in the intensities of the original peaks imply a new phase transition occurring at ~36 GPa. The main diffraction peaks, originating from the parent *Cmcm* phase or

high-pressure new HP I phase appearing at ∼6 GPa, vanish completely at ∼79 GPa with a wide coexisting pressure range of 36–79 GPa. The high-pressure phase (HP II) remains stable up to the highest pressure of ∼91 GPa in the present study. It should be noted that the diffraction reflections for the HP II phase are broad due to the stress effect. Upon decompression to ambient pressure, the high-pressure phase converts back to the initial *Cmcm* phase, showing the phase transition is reversible. The phase transition at ∼34 GPa was further confirmed at quasihydrostatic condition (Supplemental Material Figs. 9 and 10).

Using the program DICVOL, the new diffraction peaks at 91 GPa can be indexed into an orthorhombic structure and the space group is determined tentatively to be *Pmmn* according to the reflection conditions [Fig. 4(b)]. Taking the compressible behavior of the starting *Cmcm* orthorhombic phase into account, two formula units ($Z = 2$) in the unit cell are reasonably assigned for the new orthorhombic phase. The diffraction features and ratio of the lattice parameters is similar to that of the Cu_3Sb-type structure, which has structural similarity with the original *Cmcm* phase [45–48]. Based on Cu_3Sb-type structure, the x-ray diffraction pattern of the high-pressure phase of $CeTe_3$ can be well refined with the unit cell parameters of $a = 6.655(4)$ Å, $b = 4.221(3)$ Å, $c = 5.517(1)$ Å, and $V = 154.9(8)$ at 91 GPa [Fig. 4(b)]. Figure 4(c) displays the schematic crystal structure of the high-pressure *Pmmn* phase [47]. It has the orthorhombic Cu_3Sb-type structure consisting of alternate layer stacking of the Te sheets and CeTe slabs, similar to the original *Cmcm* structure. The CeTe slab has a more distorted two-layer CeTe slice, compared with the distorted NaCl-type structure slice and the Te-Ce-Te bond angle of ∼ 85° in the *Cmcm* structure [28]. On the other hand, the Te-Te bond distances along the *a* and *b* axes in the Te sheet display more discrepancy than that of the original *Cmcm* structure [Fig. 1(a)], indicating more distorted Te nets in the Te sheets for the high-pressure *Pmmn* phase. We note that the *Cmcm* structure of rare-earth tellurium compounds can be obtained by inserting a Te layer in the anti-Cu_2Sb structure ($P4/mmn$) of rare-earth telluride compounds (RTe_2) [45,46]. The high-pressure *Pmmn* structure of $CeTe_3$ has a structural relationship with RTe_2 similar to that between Cu_2Sb and Cu_3Sb. Assuming the Te atom coordinates of the *Cmcm* structure remain constant or change slightly under compression, the Te-Te bond distance between the Te layer sheets is estimated to change from ∼4.3 Å at ambient pressure to ∼3.8 Å at ∼49 GPa (Supplemental Material Fig. 11), indicating the gradual interaction enhancement of the adjacent Te sheets. It conjectures reasonably that the interlayer van der Waals force between the Te sheets evolves gradually to form the Te-Te bond under further compression and the layered structure eventually transforms into the 3D structure, namely, a 2D-to-3D structural transformation.

The pressure-dependent lattice parameters and lattice volumes for original *Cmcm* and high-pressure *Pmmn* phases are compared in Figs. 4(d) and 4(e). Generally, the lattice parameters for the *Cmcm* and HP II phases decrease with increasing pressure with anisotropic compressibility at both quasihydrostatic and nonhydrostatic conditions. Nevertheless, we notice that the lattice parameter *b* of the *Cmcm* structure exhibits anomalous compressible behavior at quasihydrostatic condition, namely, it exhibits less compressibility below 35 GPa than that at nonhydrostatic condition and decreases rather rapidly above 35 GPa. Additionally, the lattice parameter *b* shows a rapid decrease from ambient pressure to 6 GPa at quasihydrostatic conditions but displays less compressibility from 6 to 35 GPa. The same trend is observed for the lattice volumes, where the quasihydrostatic condition exhibits less compressibility below 35 GPa compared to the nonhydrostatic condition. The lattice volume under quasihydrostatic condition behaves differently below and above 6 GPa. These differences in compressible behaviors between quasihydrostatic and nonhydrostatic conditions indicate distinct paths of the structural evolution. Furthermore, the abrupt changes of the slopes in the pressure-lattice parameter and volume curves at 6 GPa imply a phase transition in the electronic structure under quasihydrostatic condition, corresponding to the suppression of CDW.

Figures 5(a) and 5(b) display the temperature-dependent resistance of $CeTe_3$ measured in the nonhydrostatic environment up to 95 GPa and down to ∼1.6 K. Starting from 1 GPa, the sample exhibits a metallic behavior as it was observed at ambient pressure. A broad hump is detected down to ∼75 K, namely, the resistance decreases upon cooling with a positive *R-T* slope from 300 to 150 K, slightly increases with a negative *R-T* coefficient from 150 to 70 K, and then decreases again below 70 K. This behavior is attributed to the effect of the CDW, consistent with previous reports [25,28]. Below 10 K, an abrupt decrease in resistance is observed in the *R-T* curve owing to an antiferromagnetic (AFM) phase [25]. Further increasing the pressure from 3.3 to 7 GPa leads to the gradual disappearance of the broad hump and AFM phase (Supplemental Material Fig. 12), accompanied by the suppression of CDW. When the CDW is suppressed completely at 7 GPa, the *R-T* curve shows the feature that the resistance decreases monotonically with a small coefficient at 100–300 K under a decrease of temperature and a large slope below 100 K, different from that at ambient pressure and 1 GPa. Meanwhile, the sample reaches zero resistance at ∼4.2 K at 3.3 GPa when the CDW began to be suppressed, suggesting the appearance of a superconducting state. The superconductivity (SC I) is confirmed by the magnetic-field suppression [49] of the superconducting transition with an upper critical field of about 2.69 T at 0 K (Supplemental Material Fig. 13). In Fig. 5(c), the superconducting transition temperature (T_c) is determined from the cross point of two straight lines above and below the transition. Upon further compression up to 17.5 GPa, the feature of an *R-T* curve exhibits the metallic behavior, similar to that at 7 GPa with a weak pressure-dependent T_c. The slope changes in the *R-T* curves, as well as the appearance of the superconductivity, indicate the occurrence of the structural transformation to the HP I phase above 7 GPa, consistent with the XRD measurement and Zocco *et al.*'s work in which a drop of resistance was observed at 2.4–5.5 K at 7–12 GPa in the Bridgman-cell experiment [25], which was attributed to a possible new phase emerging.

Another phase transition of $CeTe_3$ is implied to occur at 23–30 GPa based on the temperature-dependent resistance curves in which the slopes are different above and below the transition pressure. Above 30 GPa, the resistance decreases rapidly upon cooling from 300 to 50 K and then shows

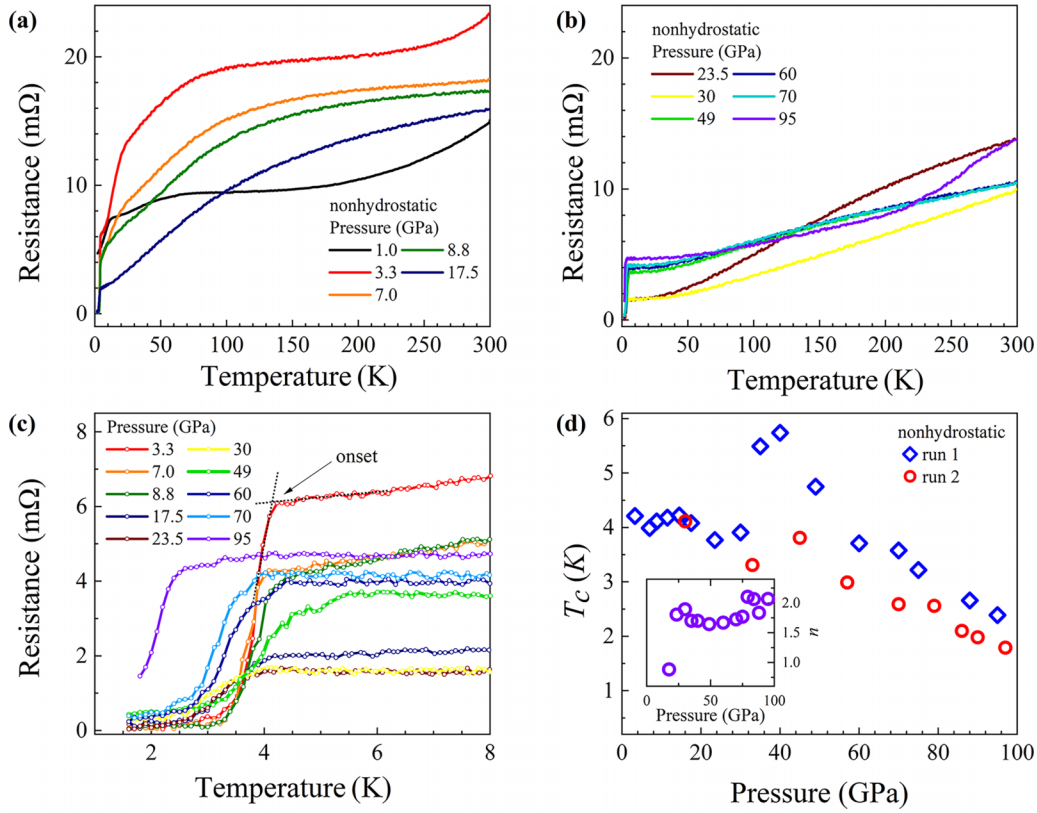

FIG. 5. (a) and (b) Temperature-dependent resistance (*R-T*) of $CeTe_3$ from 1.6 to 300 K at pressure up to 95 GPa. (c) Close-up of the *R-T* curve in the low-temperatures region of (a) and (b). The onset temperature (T_c) of superconductivity in *R-T* is defined as shown. (d) T_c as a function of pressure. The inset shows the fitting result of n between 10 and 100 K in the electric scattering model for metallic phase. The $n = 2$ means the ideal Fermi-liquid state. Both run 1 and run 2 were performed in nonhydrostatic environment and the fitting was based on the data of run 1. Pressures were determined by ruby [31] and Raman shift of diamond [37].

slight changes between 10 and 50 K. On the other hand, the electrical transport behavior between 10 and 100 K resembles the Fermi-liquid behavior of the metallic phase and the *R-T* curves in the temperature range are fitted by power law $R(T) = R_0 + AT^n$, where $n = \sim 2$ means a major contribution to conductivity from electron-electron scattering at low temperature [50]. Here, R_0 represents residual resistance at 0 K, and A is the temperature coefficient. The inset of Fig. 5(d) plots n as a function of pressure. It is observed that n increases with increasing pressure from 0.88 to ~2 under compression from 17.5 to 30 GPa. In the pressure range of 35–95 GPa, however, the n index remains nearly independent of pressure with a value close to 2. The change of n from ~0.88 to ~2 indicates a transformation of electrical transport from non-Fermi liquid to Fermi liquid [51,52] and suggests a structural phase transition. The transition is further confirmed by an anomalous change of T_c at 35–40 GPa. Above 40 GPa, T_c decreases monotonically with increasing pressure, signaling pressure-induced suppression of T_c in the HP II [Fig. 5(d)]. To further confirm the superconductive (SC II) behavior of the new phase, the suppression of the superconducting transition was examined. The superconducting transition is suppressed gradually by increasing magnetic field (Supplemental Material Fig. 13). The external magnetic-field dependent T_c at 70 GPa follows the Ginzburg-Landau formula, yielding an upper critical field of ~0.18 T at 0 K. This differs from the nature of the HP I. The phase transformation at 23–35 GPa is further confirmed by the electrical transport measurement in the second run. It should be noted that there is no hysteresis in the magnetoresistance measurement, ruing out the influences of the spin ordering on the charge transport (Supplemental Material Fig. 14).

Figure 6 displays the temperature versus pressure phase diagram of $CeTe_3$ with all measured T_c summarized. Summarily, it is clear that there are two paths for the structural evolution of $CeTe_3$ under compression, namely, structural phase transformation to *lower symmetry* at nonhydrostatic condition and anisotropic compression behavior in the Te sheets without the breaking of the structural symmetry at quasihydrostatic condition. Both ways can lead to the suppression of CDW. The XRD experiments at quasihydrostatic condition confirm that $CeTe_3$ maintains the *Cmcm* structure up to ~35 GPa. However, the CDW is suppressed at around 6 GPa, which could explain the inconsistency in the previous studies [14,25].

Of particular interest are the structural evolution and transport property of $CeTe_3$ in nonhydrostatic pressure environment, which differ from those at quasihydrostatic condition. At nonhydrostatic condition, AFM and CDW are suppressed, and an unexpected superconducting phase with T_c of 4.2 K emerges at 3.3 GPa, which corresponds to a structural phase transition from the *Cmcm* to HP I with lower symmetry. A new superconducting state, labeled by SC II, emerges at

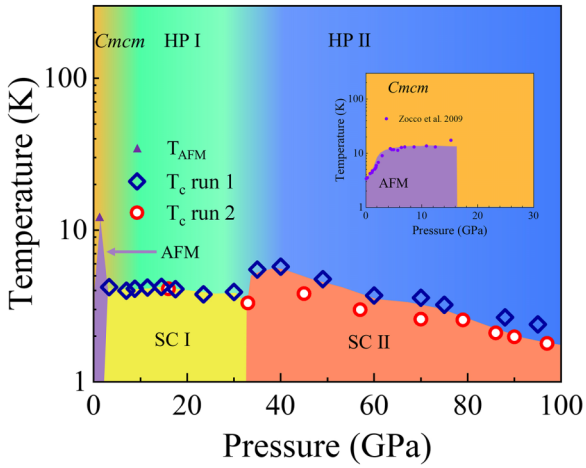

FIG. 6. Temperature vs pressure phase diagram of $CeTe_3$ summarized from the present experimental results. The inset is the diagram in the quasihydrostatic environment in which the boundary of the AFM phase is from the experimental values of Zocco *et al.* [25]. The purple diamond is the experimental value of the AFM phase transition at nonhydrostatic condition.

35 GPa with an initial T_c of 5.2 K, corresponding to the structural transition from HP I to HP II. With further compression to 40 GPa, the T_c of the SC II reaches the maximum of ~5.8 K and then decreases with increasing pressure. The SC II state corresponds to the three-dimensional *Pmmn* observed in the XRD measurements at room temperature. It is noteworthy that some layered structure materials, such as transition metal dichalcogenides, undergo the 2D to 3D structural phase transition with pressure-enhanced superconductivity [17–19,23]. It has been interpreted as the contribution of layered structure benefiting strong electron-phonon coupling [23]. Nevertheless, the results of our experiments suggest that the SC II of $CeTe_3$, which deceases with increasing pressure, may be dominated by a different electron-phonon coupling mechanism.

ACKNOWLEDGMENTS

This work was supported in part by the National Natural Science Foundation of China (Grant No. 11974033). The authors gratefully acknowledge the use of resources at the beamline 4W2 of Beijing Synchrotron Radiation Facility, and 15U1 Station, Shanghai Synchrotron Radiation Facility.

[1] K. Yumigeta, Y. Qin, H. Li, M. Blei, Y. Attarde, C. Kopas, and S. Tongay, Advances in rare-earth tritelluride quantum materials: Structure, properties, and synthesis, Adv. Sci. **8**, 2004762 (2021).

[2] J. A. Wilson, F. J. Di Salvo, and S. Mahajan, Charge-density waves and superlattices in the metallic layered transition metal dichalcogenides, Adv. Phys. **24**, 117 (1975).

[3] C. Malliakas, S. J. L. Billinge, H. J. Kim, and M. G. Kanatzidis, Square nets of tellurium: Rare-earth dependent variation in the charge-density wave of $RETe_3$ (RE = rare-earth element), J. Am. Chem. Soc. **127**, 6510 (2005).

[4] E. DiMasi, M. C. Aronson, J. F. Mansfield, B. Foran, and S. Lee, Chemical pressure and charge-density waves in rare-earth tritellurides, Phys. Rev. B **52**, 14516 (1995).

[5] N. Ru and I. R. Fisher, Thermodynamic and transport properties of YTe_3, $LaTe_3$, and $CeTe_3$, Phys. Rev. B **73**, 033101 (2006).

[6] G. F. Chen, Z. Li, D. Wu, G. Li, W. Z. Hu, J. Dong, P. Zheng, J. L. Luo, and N. L. Wang, Superconductivity at 41 K and its competition with spin-density-wave instability in layered $CeO_{1-x}F_xFeAs$, Phys. Rev. Lett. **100**, 247002 (2008).

[7] R. V. Yusupov, T. Mertelj, J.-H. Chu, I. R. Fisher, and D. Mihailovic, Single-particle and collective mode couplings associated with 1- and 2-directional electronic ordering in metallic RTe_3 (R = Ho, Dy, Tb), Phys. Rev. Lett. **101**, 246402 (2008).

[8] V. Brouet, W. L. Yang, X. J. Zhou, Z. Hussain, N. Ru, K. Y. Shin, I. R. Fisher, and Z. X. Shen, Fermi surface reconstruction in the CDW state of $CeTe_3$ observed by photoemission, Phys. Rev. Lett. **93**, 126405 (2004).

[9] A. Sacchetti, C. L. Condron, S. N. Gvasaliya, F. Pfuner, M. Lavagnini, M. Baldini, M. F. Toney, M. Merlini, M. Hanfland, J. Mesot, J.-H. Chu, I. R. Fisher, P. Postorino, and L. Degiorgi, Pressure-induced quenching of the charge-density-wave state in rare-earth tritellurides observed by x-ray diffraction, Phys. Rev. B **79**, 201101(R) (2009).

[10] M. Lavagnini, M. Baldini, A. Sacchetti, D. Di Castro, B. Delley, R. Monnier, J.-H. Chu, N. Ru, I. R. Fisher, P. Postorino, and L. Degiorgi, Evidence for coupling between charge density waves and phonons in two-dimensional rare-earth tritellurides, Phys. Rev. B **78**, 201101(R) (2008).

[11] J. A. W. Straquadine, M. S. Ikeda, and I. R. Fisher, Evidence for realignment of the charge density wave state in $ErTe_3$ and $TmTe_3$ under uniaxial stress via elastocaloric and elastoresistivity measurements, Phys. Rev. X **12**, 021046 (2022).

[12] M. Trigo, P. Giraldo-Gallo, J. N. Clark, M. E. Kozina, T. Henighan, M. P. Jiang, M. Chollet, I. R. Fisher, J. M. Glownia, T. Katayama, P. S. Kirchmann, D. Leuenberger, H. Liu, D. A. Reis, Z. X. Shen, and D. Zhu, Ultrafast formation of domain walls of a charge density wave in $SmTe_3$, Phys. Rev. B **103**, 054109 (2021).

[13] A. Zong, P. E. Dolgirev, A. Kogar, E. Ergeçen, M. B. Yilmaz, Y.-Q. Bie, T. Rohwer, I.- Cheng Tung, J. Straquadine, X. Wang *et al.*, Dynamical slowing-down in an ultrafast photoinduced phase transition, Phys. Rev. Lett. **123**, 097601 (2019).

[14] M. Lavagnini, A. Sacchetti, C. Marini, M. Valentini, R. Sopracase, A. Perucchi, P. Postorino, S. Lupi, J.-H. Chu, I. R. Fisher, and L. Degiorgi, Pressure dependence of the single particle excitation in the charge-density-wave $CeTe_3$ system, Phys. Rev. B **79**, 075117 (2009).

[15] J. Maklar, Y. W. Windsor, C. W. Nicholson, M. Puppin, P. Walmsley, V. Esposito, M. Porer, J. Rittmann, D. Leuenberger, M. Kubli, M. Savoini, E. Abreu, S. L. Johnson, P. Beaud, G. Ingold, U. Staub, I. R. Fisher, R. Ernstorfer, M. Wolf, and L. Rettig, Nonequilibrium charge-density-wave order beyond the thermal limit, Nat. Commun. **12**, 2499 (2021).

[16] M. Abdel-Hafiez, R. Thiyagarajan, A. Majumdar, R. Ahuja, W. Luo, A. N. Vasiliev, A. A. Maarouf, S. G. Zybtsev, V. Y. Pokrovskii, S. V. Zaitsev-Zotov, V. V. Pavlovskiy, W. W. Pai, W. Yang, and L. V. Kulik, Pressure-induced reentrant transition in

NbS_3 phases: Combined Raman scattering and x-ray diffraction study, Phys. Rev. B **99**, 235126 (2019).

[17] F. Yu, X. Zhu, X. Wen, Z. Gui, Z. Li, Y. Han, T. Wu, Z. Wang, Z. Xiang, Z. Qiao, J. Ying, and X. Chen, Pressure-induced dimensional crossover in a kagome superconductor, Phys. Rev. Lett. **128**, 077001 (2022).

[18] L. Yan, C. Ding, M. Li, R. Tang, W. Chen, B. Liu, K. Bu, T. Huang, D. Dai, X. Jin *et al.*, Modulating charge-density wave order and superconductivity from two alternative stacked monolayers in a bulk 4*Hb*-$TaSe_2$ heterostructure via pressure, Nano. Lett. **23**, 2121 (2023).

[19] Q. Dong, J. Pan, S. Li, Y. Fang, T. Lin, S. Liu, B. Liu, Q. Li, F. Huang, and B. Liu, Record-high superconductivity in transition metal dichalcogenides emerged in compressed 2H-TaS_2, Adv. Mater. **34**, 2103168 (2022).

[20] S. Wang, X. Chen, C. An, Y. Zhou, Y. Zhou, C. Gu, L. Zhang, X. Yang, and Z. Yang, Pressure-induced superconductivity in the quasi-one-dimensional charge density wave material CuTe, Phys. Rev. B **103**, 134518 (2021).

[21] S. Xu, J. Gao, Z. Liu, K. Chen, P. Yang, S. Tian, C. Gong, J. Sun, M. Xue, J. Gouchi, X. Luo, Y. Sun, Y. Uwatoko, H. Lei, B. Wang, and J. Cheng, Effects of disorder and hydrostatic pressure on charge density wave and superconductivity in 2*H*-TaS_2, Phys. Rev. B **103**, 224509 (2021).

[22] F. Du, S. Luo, B. R. Ortiz, Y. Chen, W. Duan, D. Zhang, X. Lu, S. D. Wilson, Y. Song, and H. Yuan, Pressure-induced double superconducting domes and charge instability in the kagome metal KV_3Sb_5, Phys. Rev. B **103**, L220504 (2021).

[23] Q. Dong, Q. Li, S. Li, X. Shi, S. Niu, S. Liu, R. Liu, B. Liu, X. Luo, J. Si, W. Lu, N. Hao, Y. Sun, and B. Liu, Structural phase transition and superconductivity hierarchy in 1T-TaS_2 under pressure up to 100 GPa, npj Quantum Mater. **6**, 20 (2021).

[24] R. Grasset, Y. Gallais, A. Sacuto, M. Cazayous, S. Mañas-Valero, E. Coronado, and M. A. Méasson, Pressure-induced collapse of the charge density wave and Higgs mode visibility in 2*H*-TaS_2, Phys. Rev. Lett. **122**, 127001 (2019).

[25] D. A. Zocco, J. J. Hamlin, T. A. Sayles, M. B. Maple, J. H. Chu, and I. R. Fisher, High-pressure, transport, and thermodynamic properties of $CeTe_3$, Phys. Rev. B **79**, 134428 (2009).

[26] J. J. Hamlin, D. A. Zocco, T. A. Sayles, M. B. Maple, J.-H. Chu, and I. R. Fisher, Pressure-induced superconducting phase in the charge-density-wave compound terbium tritelluride, Phys. Rev. Lett. **102**, 177002 (2009).

[27] D. A. Zocco, J. J. Hamlin, K. Grube, J.-H. Chu, H.-H. Kuo, I. R. Fisher, and M. B. Maple, Pressure dependence of the charge-density-wave and superconducting states in $GdTe_3$, $TbTe_3$, and $DyTe_3$, Phys. Rev. B **91**, 205114 (2015).

[28] Y. Iyeiri, T. Okumura, C. Michioka, and K. Suzuki, Magnetic properties of rare-earth metal tritellurides RTe_3 ($R = $ Ce, Pr, Nd, Gd, Dy), Phys. Rev. B **67**, 144417 (2003).

[29] See Supplemental Material at http://link.aps.org/supplemental/10.1103/PhysRevB.109.094119 for more details on EDS experiment, FFT and inverse FFT of HRTEM image, raw x-ray diffraction images, azimuthally unrolled diffraction images and optical images of sample, the FWHM fitting of Raman band and diffraction peaks, upper critical field and magnetic resistance measurements, structural evolution under pressure and extended resistance measurements with NaCl as pressure transmitting medium.

[30] S. Yesudhas, N. Yedukondalu, M. K. Jana, J. Zhang, J. Huang, B. Chen, H. Deng, R. Sereika, H. Xiao, S. Sinogeikin, C. Kenney-Benson, K. Biswas, J. B. Parise, Y. Ding, and H.-K. Mao, Structural, vibrational, and electronic properties of 1D-$TlInTe_2$ under high pressure: A combined experimental and theoretical study, Inorg. Chem. **60**, 9320 (2021).

[31] H. Deng, J. Zhang, M. Y. Jeong, D. Wang, Q. Hu, S. Zhang, R. Sereika, T. Nakagawa, B. Chen, X. Yin, H. Xiao, X. Hong, J. Ren, M. J. Han, J. Chang, H. Weng, Y. Ding, H.-Q. Lin, and H.-K. Mao, Metallization of quantum material $GaTa_4Se_8$ at high pressure, J. Phys. Chem. Lett. **12**, 5601 (2021).

[32] L. Liu, Y. Bi, and J.-A. Xu, Ruby fluorescence pressure scale: Revisited, Chin. Phys. B **22**, 056201 (2013).

[33] R. Sereika, P. Liu, B. Kim, S. Kim, J. Zhang, B. Chen, K. Yamaura, C. Park, C. Franchini, Y. Ding, and H.- K. Mao, Aberrant electronic and structural alterations in pressure tuned perovskite $NaOsO_3$, npj Quantum Mater. **5**, 66 (2020).

[34] J. Liu, High pressure x-ray diffraction techniques with synchrotron radiation, Chin. Phys. B **25**, 076106 (2016).

[35] S. Anzellini, A. Dewaele, F. Occelli, P. Loubeyre, and M. Mezouar, Equation of state of rhenium and application for ultra high pressure calibration, J. Appl. Phys. **115**, 043511 (2014).

[36] C. Prescher and V. B. Prakapenka, *DIOPTAS*: a program for reduction of two-dimensional X-ray diffraction data and data exploration, High Pressure Res. **35**, 223 (2015).

[37] A. C. Larson and R. B. Von Dreele, GSAS-II: The genesis of a modern open-source allpurpose crystallography software package, Los Alamos National Laboratory Report LAUR 86-748, 2004.

[38] Y. Akahama and H. Kawamura, Pressure calibration of diamond anvil Raman gauge to 310 GPa, J. Appl. Phys. **100**, 043516 (2006).

[39] H. J. Kim, C. D. Malliakas, A. T. Tomić, S. H. Tessmer, M. G. Kanatzidis, and S. J. L. Billinge, Local atomic structure and discommensurations in the charge density wave of $CeTe_3$, Phys. Rev. Lett. **96**, 226401 (2006).

[40] A. Tomic, Z. Rak, J. P. Veazey, C. D. Malliakas, S. D. Mahanti, M. G. Kanatzidis, and S. H. Tessmer, Scanning tunneling microscopy study of the $CeTe_3$ charge density wave, Phys. Rev. B **79**, 085422 (2009).

[41] U. Ralević, N. Lazarević, A. Baum, H.-M. Eiter, R. Hackl, P. Giraldo-Gallo, I. R. Fisher, C. Petrovic, R. Gajić, and Z. V. Popović, Charge density wave modulation and gap measurements in $CeTe_3$, Phys. Rev. B **94**, 165132 (2016).

[42] N. Lazarević, Z. V. Popović, R. Hu, and C. Petrovic, Evidence of coupling between phonons and charge-density waves in $ErTe_3$, Phys. Rev. B **83**, 024302 (2011).

[43] Y. Chen, P. Wang, M. Wu, J. Ma, S. Wen, X. Wu, G. Li, Y. Zhao, K. Wang, L. Zhang, L. Huang, W. Li, and M. Huang, Raman spectra and dimensional effect on the charge density wave transition in $GdTe_3$, Appl. Phys. Lett. **115**, 151905 (2019).

[44] M. Lavagnini, H.-M. Eiter, L. Tassini, B. Muschler, R. Hackl, R. Monnier, J.-H. Chu, I. R. Fisher, and L. Degiorgi, Raman scattering evidence for a cascade evolution of the charge-density-wave collective amplitude mode, Phys. Rev. B **81**, 081101(R) (2010).

[45] B. K. Norling and H. Steinfink, The crystal structure of neodymium tritelluride, Inorg. Chem. **5**, 1488 (1966).

[46] R. Wang, H. Steinfink, and W. F. Bradley, The crystal structure of lanthanum telluride and of tellurium-deficient neodymium telluride, Inorg. Chem. **5**, 142 (1966).

[47] C. W. Fairhurst and J. B. Cohen, The crystal structures of two compounds found in dental amalgam: Ag_2Hg_3 and Ag_3Sn, Acta. Crystallogr. **28**, 371 (1972).

[48] R. Yabune, S. Shimizu, M. Fujioka, and H. Sasaki, Effects of Ag on phase transformation of Cu_3Sb at high temperatures, J. Phys. Chem. Solids **169**, 110864 (2022).

[49] X. Liu, P. Jiang, Y. Wang, M. Li, N. Li, Q. Zhang, Y. Wang, Y.-L. Li, and W. Yang, T_c up to 23.6 K and robust superconductivity in the transition metal δ-Ti phase at megabar pressure, Phys. Rev. B **105**, 224511 (2022).

[50] M. Li, D. Zhang, J. Han, Y. Fang, N. Li, X. Liu, B. Wang, L. Yan, F. Chen, Y.-L. Li, and W. Yang, Pressure-tuning structural and electronic transitions in semimetal CoSb, Phys. Rev. B **104**, 054511 (2021).

[51] S. Kasahara, T. Shibauchi, K. Hashimoto, K. Ikada, S. Tonegawa, R. Okazaki, H. Shishido, H. Ikeda, H. Takeya, K. Hirata, T. Terashima, and Y. Matsuda, Evolution from non-Fermi- to Fermi-liquid transport via isovalent doping in $BaFe_2(As_{1-x}P_x)_2$ superconductors, Phys. Rev. B **81**, 184519 (2010).

[52] H. Takagi, B. Batlogg, H. L. Kao, J. Kwo, R. J. Cava, J. J. Krajewski, and W. F. Peck, Jr., Systematic evolution of temperature-dependent resistivity in $La_{2-x}Sr_xCuO_4$, Phys. Rev. Lett. **69**, 2975 (1992).